



HAL
open science

Hybrid numerical modelling of T-waves propagation: application to the Midplate experiment

P.-F. Piserchia, J. Virieux, D. Rodrigues, Stéphane Gaffet, J. Talandier

► **To cite this version:**

P.-F. Piserchia, J. Virieux, D. Rodrigues, Stéphane Gaffet, J. Talandier. Hybrid numerical modelling of T-waves propagation: application to the Midplate experiment. *Geophysical Journal International*, 1998, 133 (3), pp.789-800. 10.1046/j.1365-246X.1998.00546.x . hal-00497731

HAL Id: hal-00497731

<https://hal.science/hal-00497731>

Submitted on 8 Feb 2021

HAL is a multi-disciplinary open access archive for the deposit and dissemination of scientific research documents, whether they are published or not. The documents may come from teaching and research institutions in France or abroad, or from public or private research centers.

L'archive ouverte pluridisciplinaire **HAL**, est destinée au dépôt et à la diffusion de documents scientifiques de niveau recherche, publiés ou non, émanant des établissements d'enseignement et de recherche français ou étrangers, des laboratoires publics ou privés.

Hybrid numerical modelling of T -wave propagation: application to the Midplate experiment

P.-F. Piserchia,¹ J. Virieux,² D. Rodrigues,¹ S. Gaffet² and J. Talandier¹

¹ Laboratoire de Détection et de Géophysique, Commissariat à l'Énergie Atomique, 91680 Bruyères-Le-Châtel, France.

E-mail: piserchi@lgd.bruyeres.cea.fr

² Géosciences Azur, UMR 6526, CNRS-UNSA, Rue Albert Einstein, 06560 Valbonne, France

Accepted 1998 January 14. Received 1997 December 19; in original form 1997 September 5

SUMMARY

A hybrid method, coupling a ray tracing method and a finite difference approach, is proposed for modelling T -wave propagation from an underwater source to an on-land seismic station. The long-range hydroacoustic wavefield, estimated in the SOFAR channel by the Maslov approach, shows many triplications of propagation with an increasing number of caustics as the range increases. Ray tracing approaches lead to a straightforward analysis of the SOFAR propagation: we find that the duration and the amplitude of the hydroacoustic T waves generated by a source close to the SOFAR axis may be respectively eight times longer and almost seven times higher than the duration and the amplitude of hydroacoustic T waves generated by a source close to the SOFAR limits. The finite difference modelling handles the complex hydroacoustic–seismic T -wave conversion on atoll shores with an illustration of seismic T waves recorded during the Midplate experiment in 1989. Two different seismic stations, FGA on the Fangataufa Atoll and DIN on the Mururoa Atoll, both in French Polynesia, have recorded the seismic T waves due to an underwater chemical blast at a distance greater than 900 km. Synthetic seismograms computed by our proposed hybrid method are close enough to the real data for quantitative interpretation. We believe that the input model structure is accurate enough to allow such analysis of the seismic T waves. The numerical simulation shows that the seismic T waves recorded at both stations are mainly composed of P phases and Rayleigh phases. The simulation shows that the seismic T -wave duration is often linked to the source depth, although other factors (the continental slope or the distance between the top of the continental slope and the seismic station) may also affect the signal duration.

Key words: finite difference, hydroacoustic–seismic conversion, long-range propagation, ray tracing, SOFAR, T wave.

1 INTRODUCTION

The channelling efficiency of the SOFAR (for SOund Fixing And Ranging) channel allows long-range propagation of hydroacoustic waves generated by an underwater source. Here, these waves will be referred as hydroacoustic T waves. Converted hydroacoustic T waves, recorded at on-land stations, are observed after thousands of kilometres of oceanic propagation. Thus, this results in effective detection and identification capabilities for underwater sources. Hydrophone and seismic station arrays may be used to monitor underwater explosions and natural events in ocean basins. However, seismic T waves, which are converted hydroacoustic T waves, recorded at on-land stations, are often difficult to interpret.

Propagation in the ocean is an intensive area of work; some numerical approaches, normal modes, parabolic techniques, Gaussian Beam results, reflectivity results, etc. have been summarized by Jensen *et al.* (1994). However, modelling acoustic waves in a deep oceanic channel is a difficult task, particularly if the sound speed profile depends on depth and distance. One approximates the exact wavefield by an asymptotic solution calculated by the ray tracing solution. To compute a very long-range propagation in an oceanic waveguide there is no method as fast and as accurate as the ray tracing technique for a range-dependent problem, whereas computing the exact long-range propagation wavefield T waves would be excessively complicated and costly. In addition, a ray tracing approach allows straightforward

physical analysis of wavefield propagation. Ray tracing techniques have been extensively used to compute the traveltimes of acoustic multipaths of very long-range propagation (Porter 1973; Worcester 1981; Spiesberger 1994; George, Mechler & Stephan 1994).

We propose a hybrid method which takes into account the long-range wave propagation at relatively high frequencies in the SOFAR channel and the complex conversion of waves as they pass into continental areas. The ray tracing technique and its extension as the Maslov summation (Maslov 1965; Chapman 1985) are well adapted for long-distance propagation, while the finite difference method better suits the complex multiple conversion from the SOFAR propagation to continental propagation towards the on-land seismic station. A hybrid numerical modelling method, coupling both propagation techniques, is investigated, and an application to the so-called Midplate experiment organized in 1989 (Talandier 1990; Weigel 1990) shows that the overall features at the two on-land stations where seismic *T* waves were observed are recovered (Fig. 1).

Hydroacoustic wave propagation in an ocean is mainly controlled by the velocity variation with respect to depth. The velocity, which is about 1500 m s^{-1} , increases with temperature, salinity and depth (or hydrostatic pressure). The shape of the velocity curve $c(z)$, with a noticeable gradient with depth, is more important than the true value of the velocity (Fig. 2). The velocity decays rapidly with depth down to a minimum at an approximate depth of 1 km, mainly due to temperature decreases. Below this depth, the velocity increases quite linearly with hydrostatic pressure. According to ray

tracing equations, rays are continuously bent towards regions of low velocity. As shown in Fig. 2, rays are series of upward and downward arcs. Thus, the low-velocity zone is an acoustic waveguide known as the SOFAR channel and the depth of the minimum velocity is called the SOFAR axis.

A portion of energy of an underwater source located in the SOFAR channel is trapped in the waveguide, allowing propagation of waves over large distances without any reflection losses at boundaries. These waves, called hydroacoustic *T* waves, are recorded after several thousand kilometres of propagation with little decay of energy. Propagation in the SOFAR channel was first investigated by Ewing & Worzel (1948). A review of studies of propagation in the SOFAR channel can be found in Urick (1982). The envelope shape of a hydroacoustic *T* wave and its time duration are generally different from the envelope shape and the time duration of the source. After a long distance of propagation in the ocean, the hydroacoustic *T* waves hit the continental slope, leading to converted phases associated with the complex interface between the marine and continental zones. Seismic *T* waves have long been recognized, for example Gibowicz, Latter & Sutton (1974), Adams (1979) and Talandier & Okal (1987, 1996), at stations close to the coast of French Polynesia. Talandier & Okal (1997) have recently studied several cases of conversion mechanisms of seismic waves to and from hydroacoustic *T* waves in the vicinity of islands. Cansi & Bethoux (1985) were the first to use synthetic seismograms to study long inland paths of seismic *T* waves and their conversion phenomena. The complexity of the conversion phenomena is expressed by the fairly large duration of observed seismograms

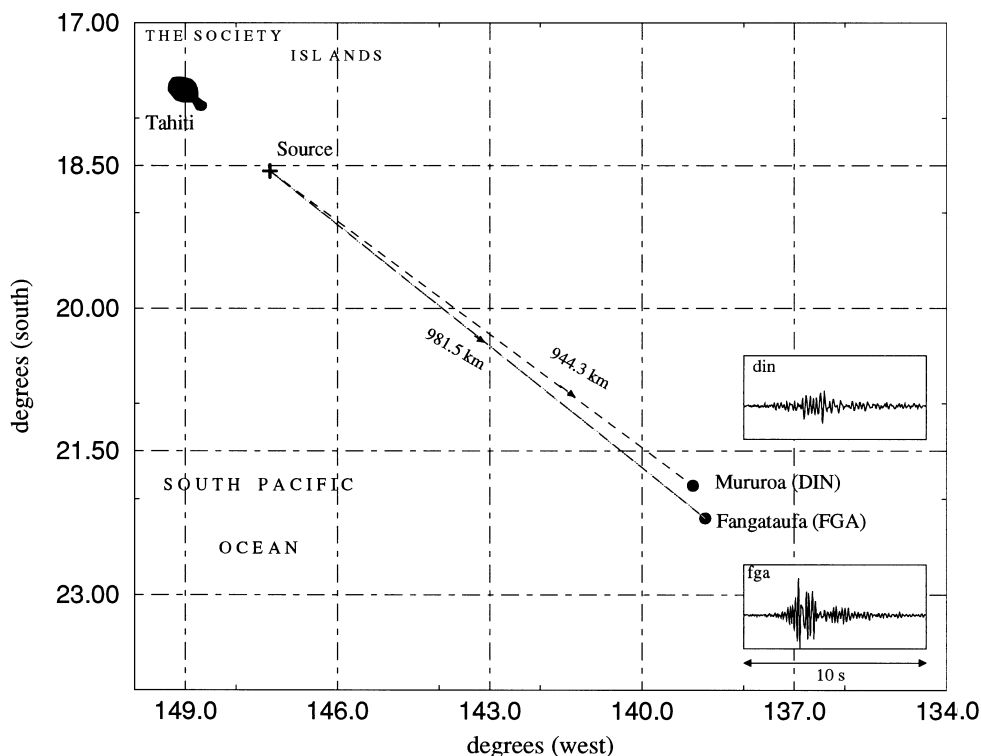


Figure 1. Map of the Midplate experiment. The explosive source was a 200 m deep chemical blast in the South Pacific Ocean. The underwater explosion generated *T* waves recorded at a distance greater than 900 km on two permanent stations. DIN is on the Mururoa Atoll and FGA is on the Fangataufa Atoll.

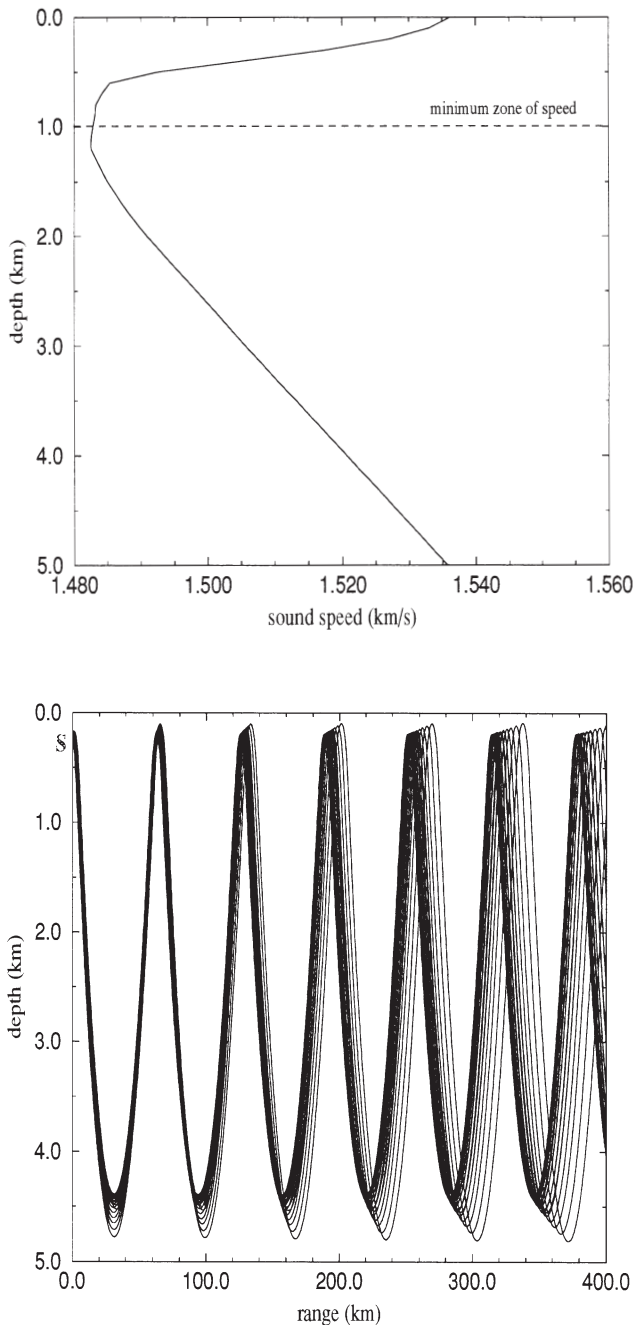


Figure 2. Hydroacoustic ray paths during the Midplate experiment. The sound speed variation had a typical vertical profile which has created a SOFAR channel. The minimum of the profile has been found around 1 km. Rays leaving the source (denoted as S) located at 200 m with a nearly horizontal take-off angle were trapped in the SOFAR channel. The T waves associated with these rays propagated over 1000 km.

(Fig. 3). The envelope shape of a seismic T wave, as well as the time duration, are often different from the envelope shape and the time duration of its 'parent' hydroacoustic T wave, because the bathymetry and the geological structure of the continental slope play a key role in the conversion phenomena (Cansi 1981). Modelling T -wave propagation from the source towards seismic stations, taking into account both the underwater

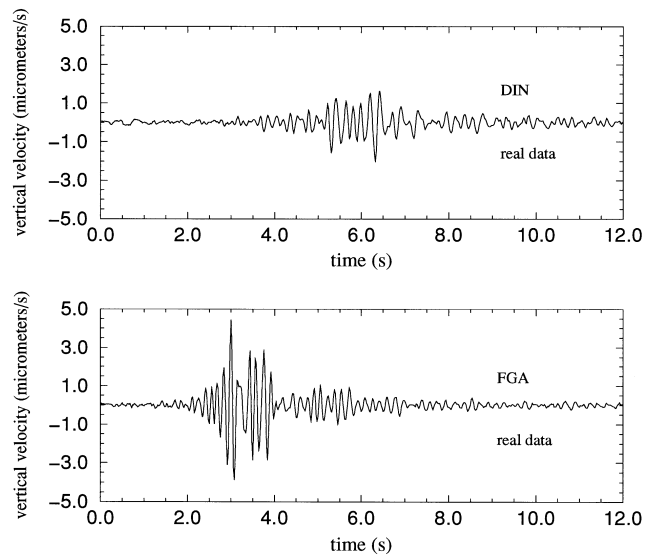


Figure 3. T waves recorded during the Midplate experiment. A shallow 200 m deep underwater explosion has generated hydroacoustic T waves, and seismic T waves have been observed at two seismic stations: DIN on the Mururoa Atoll and FGA on the Fangataufa Atoll. These two stations were respectively 981.5 and 944.3 km away from the source. Seismograms show the vertical particle velocity V_z : their timescales are identical, although their start times are arbitrary.

propagation and the elastic conversion, will be our first investigation. We will then present the Midplate experiment with an analysis of quite different seismograms at stations located at nearly the same distance (Fig. 1).

2 THE MASLOV SPECTRAL SUMMATION

Propagation over large distances of relatively high-frequency waves (frequencies and wavelengths respectively around 10 Hz and 150 m) in a smooth inhomogeneous medium such as an ocean can be performed efficiently by the ray tracing method (Jensen *et al.* 1994). An asymptotic solution is implemented, which represents accurately the exact solution when variations of the wave velocity in the ocean are smooth, like the linear gradient of velocity observed in the deep ocean (Fig. 2). Unfortunately, the existence of the SOFAR channel creates shadow zones, as well as caustics, where the asymptotic solution is either equal to zero or infinite. Then, the geometrical ray theory breaks down and other solutions must be constructed.

Whatever the computing method is, the smoothness of the wavefield is very important. In the hybrid method presented here, the excitation of the finite difference grid by waves requires a continuous wavefield in space. If this is not the case, unwanted diffraction arising from the breakdown of the wavefield would appear in the numerical grid. In order to prevent such artificial diffractions, an asymptotic spectral approach such as the Maslov summation is preferred because the wavefield will be continuous in shadow zones of the medium. According to the Liouville theorem, the volume bounded by rays in the phase space defined in terms of coordinates and slowness vector components is constant. Maslov shows that there is always a projection on a hybrid space, reducing by two the dimensions of the phase space

where no caustics are found for a given point of the phase space. The Maslov theory relies upon a clear mathematical background (Maslov 1965; Kravtsov 1968; Leray 1972). Ziolkowski & Deschamps (1984) introduced this summation in geophysics, while Chapman (1985) and Thomson & Chapman (1985) described it in seismology. Changing from the geometrical space to any hybrid space is achieved by a summation. Where the summation breaks down at hybrid caustics, the geometrical ray solution is valid away from geometrical caustics. A uniform solution, called the global solution, is obtained by combining the geometrical ray tracing and the summation using weighting factors. The global solution allows the computation at any point of a vertical section of an asymptotic continuous wavefield of the hydroacoustic T waves, generated by an underwater source in a SOFAR channel.

We summarize in the next two sections results of the geometrical ray approach and of the Maslov summation.

2.1 The geometrical ray tracing solution

Let us consider the scalar field u_r which represents the radial motion defined as the amplitude of the motion (u_x, u_z). In a heterogeneous oceanic medium, the wavefield excited by an underwater explosive point source satisfies (Jensen *et al.* 1994)

$$\text{div}[k(\mathbf{X}) \text{grad}(u_r(\mathbf{X}, t)) - \rho(\mathbf{X}) \partial_{tt}^2 u_r(\mathbf{X}, t)] = -f_s(t) \delta(\mathbf{X}). \tag{1}$$

The source is located at $\mathbf{X}=\mathbf{O}$, where the density and the velocity are respectively equal to ρ_0 and c_0 . The source time function of the point force is denoted as $f_s(t)$. The bulk modulus is related to density $\rho(\mathbf{X})$ and velocity $c(\mathbf{X})$ by the well-known relation

$$k(\mathbf{X}) = \rho(\mathbf{X}) c^2(\mathbf{X}). \tag{2}$$

We define the time Fourier transform F of a generic function f by

$$F(\omega) = \int_{-\infty}^{+\infty} f(t) e^{i\omega t} dt, \quad f(t) = \frac{1}{2\pi} \int_{-\infty}^{+\infty} F(\omega) e^{-i\omega t} d\omega, \tag{3}$$

and the spatial Fourier transform by

$$F(k_z) = \int_{-\infty}^{+\infty} f(z) e^{-ik_z z} dz, \quad f(z) = \frac{1}{2\pi} \int_{-\infty}^{+\infty} F(k_z) e^{ik_z z} dk_z. \tag{4}$$

The Hilbert transform of f , denoted as f_h , has its time Fourier transform expressed as

$$F_h(\omega) = -i \text{sign}(\omega) F(\omega) = \exp[-i(\pi/2) \text{sign}(\omega)] F(\omega). \tag{5}$$

The analytic transform f_a of f is defined as $f_a(t) = f(t) + if_h(t)$. The asymptotic motion ($u_x^{\text{grt}}, u_z^{\text{grt}}$) at a receiver point \mathbf{X} provided by the geometrical ray tracing (superscript grt) may be simply written in the time domain as follows:

$$u_x^{\text{grt}}(\mathbf{X}, t) = \sum_{\text{rays}} \cos(\theta) u_r(\mathbf{X}, t), \tag{6}$$

$$u_z^{\text{grt}}(\mathbf{X}, t) = \sum_{\text{rays}} \sin(\theta) u_r(\mathbf{X}, t). \tag{7}$$

The summation is performed over rays which arrive at the receiver. Cartesian components of the motion will be applied

to the finite difference grid. Consequently, the angle θ is the angle between the ray and the horizontal. Each elementary contribution is given by

$$u_r(\mathbf{X}, \omega) = A(\mathbf{X}, \theta_0) F_s(\omega) e^{i\omega T(\mathbf{X})} e^{-i \text{kmah}(\mathbf{X}) \pi / 2} \tag{8}$$

in the frequency domain, and may be written in the time domain as

$$u_r(\mathbf{X}, t) = A(\mathbf{X}, \theta_0) \mathcal{R}_e[(-i)^{\text{kmah}} f_a(t)]. \tag{9}$$

The kmah index (for Keller, Maslov, Arnold, Hörmander), the number of caustics crossed by a ray, initially equal to zero, increases by one every time the ray hits a caustic. In a 3-D medium the amplitude term $A(\mathbf{X}, \theta_0)$ is

$$A(\mathbf{X}, \theta_0) = A_0(\theta_0) \sqrt{\frac{1}{J_z(\mathbf{X}) \rho(\mathbf{X}) c(\mathbf{X})}}. \tag{10}$$

For a 3-D isotropic point source radiation, the amplitude term $A_0(\theta_0)$ at the source is given by

$$A_0(\theta_0) = \frac{1}{4\pi \rho_0 c_0^2} \sqrt{|\cos(\theta_0)| \rho_0 c_0}, \tag{11}$$

while for a 3-D cylindrically symmetric medium the Jacobian $J(\mathbf{X})$ is estimated by

$$J_z(\mathbf{X}) = |x| \left| c(\mathbf{X}) \mathbf{p} \wedge \frac{\partial \mathbf{X}}{\partial \theta_0} \right|, \tag{12}$$

where the distance x , the slowness vector \mathbf{p} and the partial derivative $\partial \mathbf{X} / \partial \theta_0$ are computed along rays. The traveltime T and the initial take-off angle θ_0 complete our definition. The slowness vector \mathbf{p} makes an angle θ with the horizontal. The distance x controls the lateral spreading and $|c(\mathbf{X}) \mathbf{p} \wedge \partial \mathbf{X} / \partial \theta_0|$ is related to the 2-D spreading. The inverse time Fourier transform of ($u_x^{\text{grt}}(\mathbf{X}, \omega), u_z^{\text{grt}}(\mathbf{X}, \omega)$) provides a zeroth-order solution of the wave equation (1) in the geometrical space denoted by (x, y, z, t) .

2.2 The Maslov summation

Let us define the hybrid space by taking the space Fourier transform of the z -coordinate. Following Chapman (1985), the Maslov seismograms ($u_x^{\text{mas}}, u_z^{\text{mas}}$) are obtained in the geometrical space by first taking the inverse time Fourier transform of a zeroth-order solution in the Snell space and then taking the inverse spatial Fourier transform in the coordinate z . The solution is a time convolution through the following expression:

$$u_x^{\text{mas}}(\mathbf{x}, t) = -\mathcal{R}_e \left[\frac{1}{\pi \sqrt{2}} \frac{\partial f_a(t)}{\partial t} * \lambda_h(t) * \int_{\theta_0^{\text{min}}}^{\theta_0^{\text{max}}} (-i)^\nu B(x, y, \theta_0) \times \cos(\theta) \delta(t - \mathcal{F}(x, y, z, \theta_0)) d\theta_0 \right], \tag{13}$$

$$u_z^{\text{mas}}(\mathbf{x}, t) = -\mathcal{R}_e \left[\frac{1}{\pi \sqrt{2}} \frac{\partial f_a(t)}{\partial t} * \lambda_h(t) * \int_{\theta_0^{\text{min}}}^{\theta_0^{\text{max}}} (-i)^\nu B(x, y, \theta_0) \times \sin(\theta) \delta(t - \mathcal{F}(x, y, z, \theta_0)) d\theta_0 \right]. \tag{14}$$

The Maslov index γ is related to the kmah index by

$$\gamma(\mathbf{X}) = \text{Ind} \left(\frac{\partial p_z}{\partial z} \right)_{x=\text{cte}} + \text{kmah}(\mathbf{X}). \quad (15)$$

The function Ind is defined as $\text{Ind}(u) = 1$ if $u < 0$ and $\text{Ind}(u) = 0$ if $u \geq 0$. Writing H as the Heaviside function, recall that $\lambda_h(t) = H(-t)(-t)^{-1/2}$ is the Hilbert transform of the function $\lambda(t) = H(t)t^{-1/2}$. Finally, the function f_a is the analytic transform of f , and δ is the delta function, making the double convolution simpler to estimate numerically.

The geometrical ray tracing parameters used in the Maslov summation are the time function $\mathcal{F}(x, y, z, \theta_0)$ and the amplitude B . The time function \mathcal{F} is related to the intercept time τ by the relation

$$\mathcal{F}(x, y, z, \theta_0) = \tau(x, y, \theta_0) + p_z(\theta_0)z, \quad (16)$$

with the following definition of the τ function:

$$\tau(x, y, \theta_0) = T(x, y, z(\theta_0)) - p_z(\theta_0)z(\theta_0), \quad (17)$$

which is the Legendre transform connecting the ray travel-time T to the plane-wave traveltime τ . The Maslov integration (eqs 13 and 14) may be considered as a plane-wave summation over θ_0 .

The amplitude term is

$$\begin{aligned} B(x, y, \theta_0) &= A_0(\theta_0) \frac{\partial p_z}{\partial \theta_0} \sqrt{\frac{1}{J_{p_z} \rho(\mathbf{x}) c(\mathbf{x})}} \\ &= A_0(\theta_0) \text{sign} \left(\left(\frac{\partial p_z}{\partial \theta_0} \right)_x \right) \sqrt{\frac{1}{\left| \frac{\partial(x, y)}{\partial(s, \phi_0)} \right| \left| \frac{\partial \theta_0}{\partial p_z} \right|_x \rho(\mathbf{x}) c(\mathbf{x})}}, \end{aligned} \quad (18)$$

where $J_{p_z} = J_z \partial p_z / \partial \theta_0$, ϕ_0 is the declination angle and s is the arc length. When the velocity structure of the 3-D medium is cylindrically symmetric with respect to the z -axis the determinant $\partial(x, y) / \partial(s, \phi_0) = x p_x c(\mathbf{x})$ is expressed analytically. The distance $|x|$ from the source to the station and the slowness p_x control the lateral extension and the 2-D extension of the ray tube.

From the relation between J_{p_z} and J_z , it can be deduced that, whereas the geometrical ray amplitude is infinite on geometrical caustics, the amplitude of the Maslov summation is zero on hybrid caustics. The geometrical ray tracing and the Maslov summation never fail at the same position. We need to construct a global asymptotic solution, which will be denoted u^{glo} , valid at each point in the medium.

2.3 A global solution

The global solution is tentatively constructed from the solution u^{grt} of the geometrical ray tracing and from the Maslov summation u^{mas} . The local slopes $\partial z / \partial \theta_0$ and $\partial p_z / \partial \theta_0$ allow one to control the distance to caustics on the hybrid space and on the geometrical space: the partial derivative $\partial z / \partial \theta_0$ equal to zero defines caustics on the geometrical space, while the partial derivative $\partial p_z / \partial \theta_0$ equal to zero defines caustics on the hybrid space (Fig. 4). Let w^{grt} and w^{mas} define two weighting functions such that they are respectively equal to zero on a caustic in the geometrical space and in the hybrid space, while their sum $w^{\text{grt}} + w^{\text{mas}}$ stays equal to one. The global solution u^{glo} is

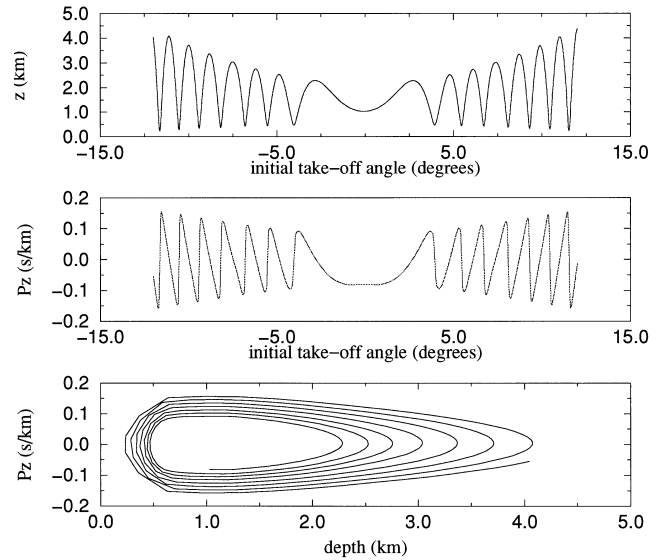


Figure 4. Set of diagrams showing wave-front information in a vertical section. Note the high number of geometrical and hybrid caustics found during the hydroacoustic T -wave propagation. The source is 500 m deep and the receivers are in a vertical section 980 km away from the source. The local slopes $\partial z / \partial \theta_0$ and $\partial p_z / \partial \theta_0$ allow control of the distance to caustics in the hybrid space and in the geometrical space. Caustics are also characterized on the curves $p_z(z)$. For clarity, only points (z, p_z) associated with negative initial take-off angles are plotted. The partial derivative $\partial p_z / \partial z$ is infinite at geometrical caustics and equal to zero at hybrid caustics.

defined as

$$\begin{aligned} u_x^{\text{glo}}(\mathbf{x}, t) &= \sum_{\text{rays}} w^{\text{grt}}(x, y, \theta_0) \cos(\theta) A(x, y, \theta_0) \\ &\quad \times \Re e [(-i)^{\text{kmah}} f_a(t)] + \Re e \left[\frac{-1}{\pi \sqrt{2}} \frac{\partial f_a(t)}{\partial t} * \lambda_h(t) \right. \\ &\quad * \int_{\theta_0^{\text{min}}}^{\theta_0^{\text{max}}} w^{\text{mas}}(x, y, \theta_0) \cos(\theta) B(x, y, \theta_0) (-i)^{\gamma} \\ &\quad \left. \times \delta(t - \tau(x, y, z, \theta_0)) d\theta_0 \right], \end{aligned} \quad (20)$$

$$\begin{aligned} u_z^{\text{glo}}(\mathbf{x}, t) &= \sum_{\text{rays}} w^{\text{grt}}(x, y, \theta_0) \sin(\theta) A(x, y, \theta_0) \\ &\quad \times \Re e [(-i)^{\text{kmah}} f_a(t)] + \Re e \left[\frac{-1}{\pi \sqrt{2}} \frac{\partial f_a(t)}{\partial t} * \lambda_h(t) \right. \\ &\quad * \int_{\theta_0^{\text{min}}}^{\theta_0^{\text{max}}} w^{\text{mas}}(x, y, \theta_0) \sin(\theta) B(x, y, \theta_0) (-i)^{\gamma} \\ &\quad \left. \times \delta(t - \tau(x, y, z, \theta_0)) d\theta_0 \right]. \end{aligned} \quad (21)$$

The discrete summation is performed over rays which arrive at the receiver. The global solution is such that when the position is close to a caustic in the geometrical space, the wavefield is mainly computed by the Maslov summation, and when the position is near a caustic in hybrid space, the wavefield is mainly estimated by geometrical ray tracing. The weighting functions should be functions of the partial derivatives $\partial z / \partial \theta_0$ and $\partial p_z / \partial \theta_0$, which take finite values on caustics. How to choose these functions is still an open question (Huang &

West 1997). In the next section, the weighting functions are defined as

$$w^{\text{grt}}(x, y, \theta_0) = \frac{b_1(\partial z/\partial\theta_0)^2}{b_1(\partial z/\partial\theta_0)^2 + b_2(\partial p_z/\partial\theta_0)^2}, \quad (22)$$

$$w^{\text{mas}}(x, y, \theta_0) = \frac{b_2(\partial p_z/\partial\theta_0)^2}{b_1(\partial z/\partial\theta_0)^2 + b_2(\partial p_z/\partial\theta_0)^2}. \quad (23)$$

The two normalization constants b_1 and b_2 are introduced because the quantities $\partial z/\partial\theta_0$ and $\partial p_z/\partial\theta_0$ are different. Their values control the weighting functions (Huang & West 1997; Piserchia *et al.* 1997). Making an asymptotic development of eqs (20) and (21), it can be shown that the global solution is still an asymptotic solution of the wave equation, whatever the choice of weighting functions and in particular whatever the choice of normalization constants. For the modelling of the Midplate experiment, presented in the next section, b_1 equals zero and b_2 equals one. Because the sound speed is very slowly varying, the effects of hybrid caustics are negligible (Piserchia *et al.* 1997).

The medium is described by a B-spline interpolation in both the vertical and the horizontal coordinates [see Virieux (1991) and Virieux & Farra (1991) for the B-spline application to ray tracing]. A paraxial method (Farra & Madariaga 1987; Virieux, Farra & Madariaga 1988) in Cartesian coordinates can be used to compute accurately partial derivatives with respect to the variable θ_0 along the ray (partial derivatives $\partial z/\partial\theta_0$, $\partial p_z/\partial\theta_0$ and $\partial \mathbf{X}/\partial\theta_0$ for example). From these partial derivatives, a systematic detection of caustics is possible using the kmah index. Of course, other failures such as shadow zones or global boundaries of the medium will separate ray branches. Rays which belong to the same ray branch have the same interaction with the medium (same number of surface and bottom reflections, same number of transmissions and so on) and the same kmah index. The branch structure defined at a constant range will be called a z -branch.

3 HYDROACOUSTIC T -WAVE PROPAGATION

3.1 The Midplate experiment

In December 1989, J. Talandier co-organized a seismic experiment, called the Midplate experiment, in the French Polynesia islands in order to investigate T -wave conversion over the Pacific Ocean (Fig. 1). The explosive source was a 300 kg chemical blast of geosite located to the SE of Tahiti in the South Pacific Ocean, in the vicinity of the Society Islands. The source was close to a depth of 200 m. The underwater explosion generated hydroacoustic T waves and seismic T waves, which were observed in particular at two permanent seismic stations. These two stations were nearly at the same distance: DIN on Mururoa Atoll at a distance of 944.3 km and FGA on Fangataufa Atoll at a distance of 981.5 km. Both receivers recorded the vertical particle velocity in a range of frequencies between 2 and 10 Hz (Fig. 3), with a central frequency of 6 Hz. A time–frequency analysis shows that the observed seismic T waves are not dispersive in the frequency range 2–10 Hz. We choose to represent the source time function as a unit normalized Ricker wavelet with the main frequency equal to 6 Hz. We note that the global shape, the

duration, the maximum amplitude and the energy of these two recorded seismic T waves (Fig. 3) are different, even though the propagation in the ocean and in the geological structure of both atolls seems very similar (Fig. 5). During the Midplate experiment, the sound speed variation (Fig. 2) had a typical vertical profile creating a SOFAR channel. The minimum velocity axis is at a depth of nearly 1 km. We assume that during this experiment the ocean may be considered as a plane stratified medium from the source to the receiver with only vertical variations in the medium properties.

Both geometrical ray tracing and Maslov summation were used to compute synthetic hydroacoustic T waves. We shall concentrate our attention on hydroacoustic T waves from a shallow 200 m depth source close to the upper SOFAR channel limit, as done during the Midplate experiment, and from a 500 m source closer to the channel axis. Fig. 6 illustrates clearly that the amplitude and the signal duration are very different for a source located near the SOFAR channel limit and for a source closer to the channel axis. Because of the straightforward physical analysis of the ray methods, we can argue that the amplitude, the number of z -branches, the extension of the duration and the envelope shape are associated with the depth of the source and the depth of the receiver.

3.2 The flux of the trapped energy

Only a part of the source energy is trapped in the SOFAR channel. Indeed, if the initial take-off angle of a ray is too high, it will not be guided in the SOFAR channel. Only rays with an initial take-off angle between $-\theta_c$ and $+\theta_c$ are trapped in the SOFAR channel and propagate without encountering reflection losses at the sea surface or seafloor. The critical angle θ_c varies with the source depth z_s and the sound speed c_1 at the

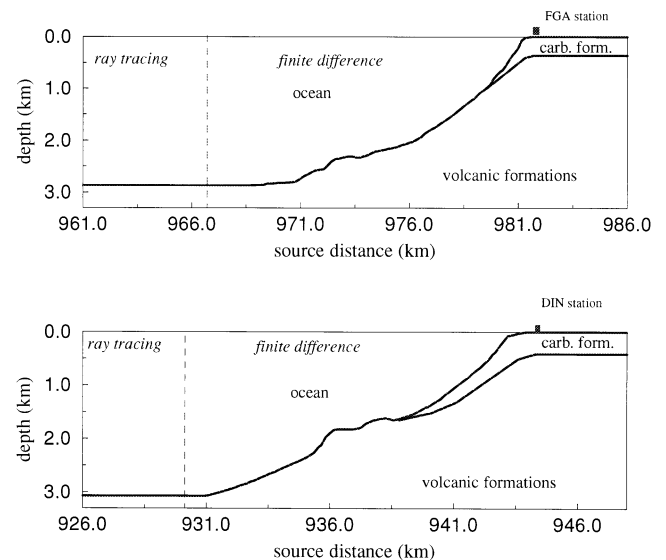


Figure 5. The main geological units of the continental slopes at both FGA and DIN are volcanic formations ($v_p = 3400 \text{ m s}^{-1}$, $v_s = 1963 \text{ m s}^{-1}$, $\rho = 2350 \text{ kg m}^{-3}$) and carbonate formations ($v_p = 2800 \text{ m s}^{-1}$, $v_s = 1617 \text{ m s}^{-1}$, $\rho = 2270 \text{ kg m}^{-3}$). The coupling borderlines (dashed lines) between the ray tracing and the finite difference computation are 966 km from the source at FGA and 929 km at DIN.

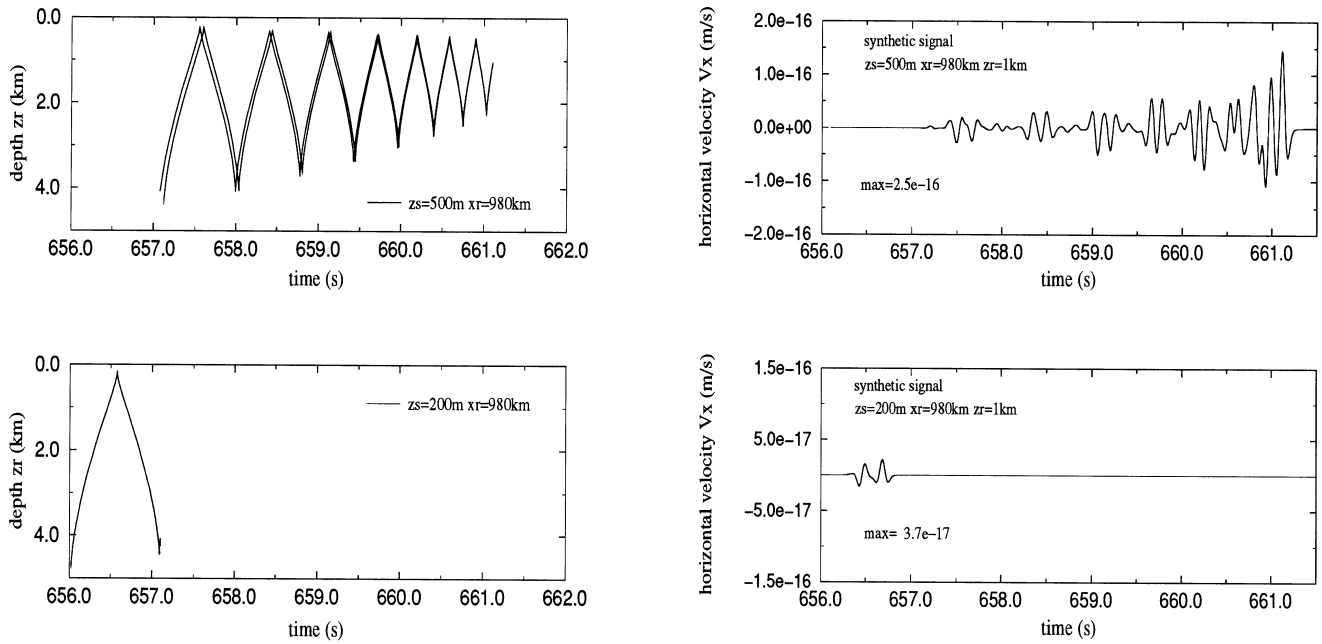


Figure 6. Hydroacoustic propagation. The source time function is a unit normalized Ricker wavelet with main frequency equal to 6 Hz. The left panels show two traveltimes curves computed in a vertical section 980 km away from the source. For the top panel the source is 500 m deep and for the bottom panel the source is 200 m deep. The traveltimes curves are split into several z -branches. When the source becomes closer to the SOFAR channel axis, the number of z -branches increases and the signal duration for a given receiver becomes longer as can be seen on the right panels with corresponding source depths from the left panels. The receiver position is 1 km deep right on the SOFAR channel axis.

limit of the SOFAR channel according to the relation

$$\theta_c = \arcsin(c_s(z_s)/c_1). \quad (24)$$

If the sea surface is considered as the upper SOFAR channel limit, c_1 is the sound speed at the surface. The highest value of the critical angle is found when the source is on the SOFAR channel axis. The critical angle tends to zero when the source is close to the upper or the lower SOFAR channel limit. For an isotropic explosion the percentage of trapped energy in one direction at the point source may be defined as $\sin \theta_c$. When all the energy is guided in the SOFAR channel, the critical angle is equal to $\pi/2$ and the proportion of trapped energy is a maximum and is equal to 100 per cent. Fig. 7 shows that the trapped flux depends on the source depth but is generally not linearly varying with depth. Note that the seafloor interaction, as well as the surface interaction, are not taken into account. Fig. 7 illustrates clearly why the energy recorded at a given underwater receiver, after long-range propagation, may be very different for a shallow source and for a source closer to the SOFAR channel axis. It also explains why the energy and amplitude recorded at a seismic station depend on the source depth. The trapped flux reaches a maximum close to 16 per cent when the source is on the SOFAR channel axis; it tends to zero when the source is close to the surface or the seafloor.

3.3 Caustics and z -branches

The traveltimes curve $T(z)$ which provides an image of the wave front is split into 30 z -branches along a vertical cross-section 980 km away from the 500 m depth source and into six z -branches when the source is 200 m deep (Fig. 6). These z -branches are separated by caustics at turning points of the traveltimes curve. Fig. 8 shows traveltimes, depths and the

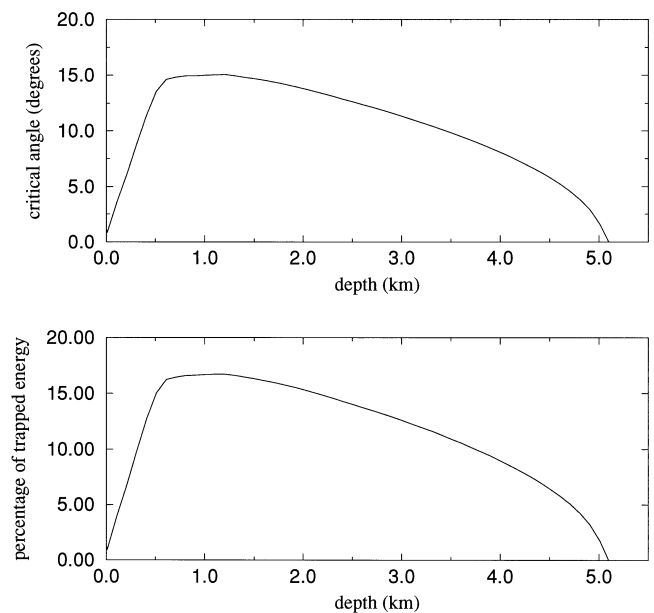


Figure 7. Variation with depth of the critical angle and the trapped energy during the Midplate experiment. The trapped flux is at a maximum when the source is on the SOFAR channel axis; it tends to zero when the source is close to the surface or the seafloor. The variation with depth does not follow a linear rule.

kmah index (number of caustics crossed by a ray) with respect to the initial take-off angle of the ray for receivers in a fixed vertical plane. At any receiver taken on the vertical plane, the wavefield is constructed by the summation of the elementary contributions of rays. Each extremum of the curve $z(\theta_0)$ is a

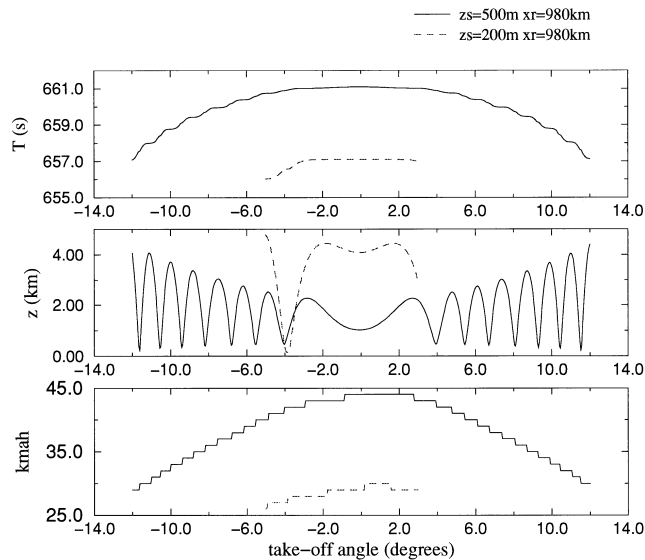


Figure 8. Influence of the initial take-off angle. Each ray is defined by its take-off angle. The smaller the take-off angle θ_0 , the higher the kmah index (number of caustics crossed by a ray) and the later the arrival time. An extremum of the curve $z(\theta_0)$ is connected to a saddle point of $T(\theta_0)$ and a unit variation of $\text{kmah}(\theta_0)$.

depth where a geometrical caustic is passed through. The kmah index is accordingly increased by a value of one. The number of caustics crossed by a ray decreases when the take-off angle increases. A ray travelling close to the SOFAR channel axis crosses many more caustics than a ray which propagates near the limits of the SOFAR channel.

3.4 The envelope shape: duration and amplitude

When both source and receivers are closed to the channel axis, the synthetic T -wave envelope has a typical shape. The recorded signal is quite long (time duration 4 s) and gradually increases, reaching a peak, and then stops abruptly (Fig. 6). The front end of the signal represents contributions of rays which travel near the SOFAR channel axis, making many oscillations around the axis. The rear end of the signal is due to rays leaving the source with a higher take-off angle going up and down near the limits of the SOFAR channel, where the sound speed value is at a maximum. The first arriving rays are rays leaving the source with a high take-off angle, while the last arrivals are rays leaving the source with a small take-off angle. The signal has a smooth build-up because the density of rays and their elementary amplitude contribution increase with time. Fig. 6 shows that the number of arrivals per time unit is increasing with the duration because the gap between z -branches is decreasing. At the same 1 km deep receiver, the envelope shape stays simpler for a shallower source at a depth of 200 m. The signal is 0.5 s long with two noticeable variations associated with a small number of contributions from rays which pass near the channel limits.

Hydroacoustic T -wave synthetics in Fig. 6 show that the signal duration observed at constant range depends on the source depth. Fig. 9 illustrates the variation of the hydroacoustic T -wave duration with the source depth at receivers parametrized by their distance x_r from the source. When a

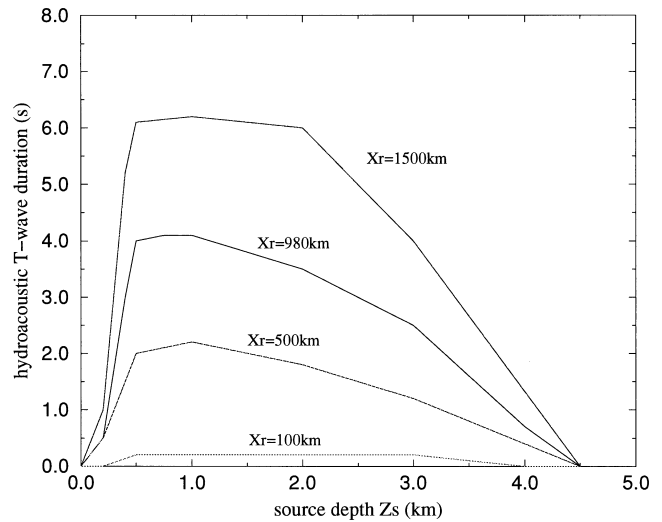


Figure 9. Hydroacoustic T -wave duration. As the source gets closer to the SOFAR channel, the hydroacoustic T -wave duration recorded at the receiver increases. The source is 980 km from the receiver, which has a depth of 1 km. The extension of the signal duration may be considered proportional to the distance when the receiver is far enough from the source ($x_r = 1500$ km, $x_r = 980$ km, $x_r = 500$ km). When the receiver comes closer to the source, the signal duration tends towards the source duration, which is about 0.2 s for our source model. At a 1 km deep receiver located at 100 km from the source, the signal duration is equal to 0.2 s whatever the source depth (except when receivers are located in a shadow zone).

receiver is farther from the source than a reference range, the signal duration at the receiver may be considered proportional to the signal duration at the reference range. This property is best established when the source is close to the SOFAR channel axis, the receiver is far from the source and the SOFAR channel is slowly varying with range. The reference range must be far enough from the source to allow many ray oscillations around the axis. For the practical geometry we are studying (Fig. 9), the reference range should be greater than 500 km. When the receiver is closer to the source, the signal duration approaches the source duration, which is about 0.2 s for the specified source.

4 A HYBRID METHOD COUPLING THE RAY TRACING AND THE FINITE DIFFERENCE SIMULATIONS

For the long-range propagation of hydroacoustic T -waves in the SOFAR channel, the asymptotic approach based on geometrical ray tracing and its Maslov summation extension provide a fast and accurate method. Unfortunately, conversion to seismic T waves on a continental slope with complex conversions such as diffraction or interface waves cannot be taken into account by ray theory. An alternative might be the choice of a numerical method such as the finite difference approach in the domain where the continental slope is involved.

The finite difference method discretizes and solves the wave equation from given initial conditions and boundary conditions. At each time step of the algorithm, the wavefield is computed at each node of a given grid representing the propagation medium. This technique takes complex phenomena into account, but has its own limits. As a rule of

thumb, the wavefield could not be propagated at distances larger than a few hundred times the smallest wavelength without noticeable numerical dispersion developing. In a medium with an S -wave velocity of 2000 m s^{-1} the extension of the domain could not exceed a few tens of kilometres. Overcoming this limitation, although possible, would require intensive computer resources. This is why we propose both ray tracing and finite difference methods for solving the long-range propagation of T waves.

4.1 A hybrid strategy

The propagation from the underwater source of the hydroacoustic wavefield over a long range in the SOFAR channel is performed by ray tracing techniques until waves arrive near the continental slope. We estimate the wavefield on a vertical boundary line and start the propagation by a finite difference method in the zone of the continental slope towards the seismic land station. Each method of propagation modelling is applied in its own domain of interest and validity. The medium is subdivided into two areas. The first contains the underwater source and the SOFAR channel while the second contains the continental slope and the seismic station. These two areas are separated by the vertical borderline.

A finite difference code simulates the propagation into a heterogeneous medium in a 2-D geometry or in an axisymmetric geometry. We use a code that runs on massively parallel computers and has high-order finite difference estimations of partial derivatives (Rodrigues 1993). We have used an order of eight in space and four in time in our simulations in order to minimize the numerical dispersion. The mixed method we propose will be called the hybrid method.

4.2 The coupling technique

The excitation of the finite difference numerical grid by the ray tracing solution can be performed by different strategies. We briefly describe the two methods we use.

4.2.1 A forced coupling

In this coupling technique, the ray tracing method estimates the wavefield motion at every node of the grid in the coupling domain of the discretized medium. Taking into account the spatial order of the finite difference scheme, the vertical coupling domain will extend horizontally in such a way that the wavefield in the coupling domain can be used as an initial condition for the finite difference computation. The spatial differential operator is an eighth-order scheme, requiring a coupling grid of seven horizontal nodes and all vertical nodes of the discretized grid.

This coupling method, called a forced coupling, has been successfully tested. We consider only the SOFAR channel medium over a horizontal distance of 20 km. A coupling domain is taken 10 km away from the source. The underwater source is 2 km deep, while receivers are at three different depths, 0, 2 and 4 km. We compute three solutions: the first with only the ray theory, the second with the finite difference method and the third with the hybrid approach. Wavefields are indistinguishable whatever the method selected, as shown in Fig. 10. In this numerical experiment, we have fulfilled the conditions required by both methods to be valid.

4.2.2 A Green function coupling

Another alternative for the coupling between the ray tracing and finite difference methods can be achieved by the Representation Theorem (Rodrigues 1996). This coupling, which we call a Green function coupling, is well suited for source parameter studies. We estimate the wavefield motion $u = (u_x, u_z)$ and the tensor σ due to the underwater source by geometrical ray tracing in a vertical section Γ in the coupling domain. In the same section Γ , the Green functions G^x and G^z and the tensors σ^{G^x} and σ^{G^z} , due respectively to a horizontal and a vertical impulse force at the receiver (x_r, z_r) , are estimated by the finite difference technique. Both simulations are independent and are related only through the results over the Γ section. The Representation Theorem allows one to compute the wavefield motion generated by the source at the receiver knowing the wavefield motion $u = (u_x, u_z)$ and the Green functions G^x and G^z in the Γ section by

$$u_x(x_r, z_r, t) = \int_{\Gamma} (G^x * (\sigma \cdot n_{\Gamma}) - u * (\sigma^{G^x} \cdot n_{\Gamma})) d\Gamma, \quad (25)$$

$$u_z(x_r, z_r, t) = \int_{\Gamma} (G^z * (\sigma \cdot n_{\Gamma}) - u * (\sigma^{G^z} \cdot n_{\Gamma})) d\Gamma, \quad (26)$$

where n_{Γ} is the normal to Γ . The computer-intensive modelling by the finite difference method needs to be performed only once. Any modification of the source parameters such as the horizontal distance and the depth of the source can be taken into account very efficiently by the ray tracing approach. A parametric study of an unknown underwater source can thus be performed using this Green function coupling.

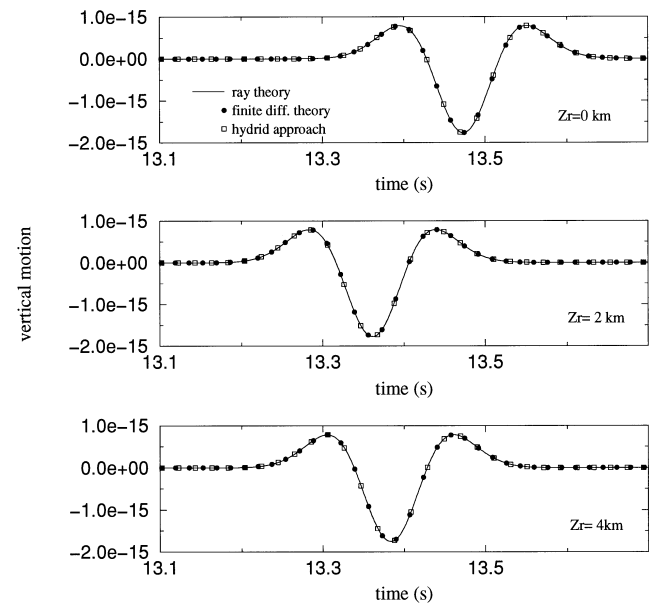


Figure 10. Comparison between the ray tracing approach, the finite difference technique and the hybrid method in the SOFAR channel without continental slope. The velocity is a linear function of depth [$c(z) = 1.5 + 0.005z \text{ km s}^{-1}$], while the density stays constant ($\rho = 1000 \text{ kg m}^{-3}$). The vertical motion computed by a direct method and by the hybrid method is compared for three different depths of recording. The source is 2 km deep with a time function taken as a unit normalized Ricker function with a central frequency of 5 Hz. The receivers are 20 km away from the source.

5 SEISMIC *T*-WAVE CONVERSION

For the Midplate experiment, ray modelling was first performed from the explosive source towards the two stations. At 15.5 km distance from DIN we stopped the ray modelling and kept the wavefield for a forced coupling of the finite difference grid. We performed the same modelling for FGA and kept the wavefield at a distance of 15.3 km. Hydroacoustic *T*-wave propagation has been performed by Maslov summation in an axisymmetric vertically varying medium defined in Fig. 2.

Because the lateral geometrical spreading due to the final part of the propagation is small compared to the long-range oceanic lateral geometrical spreading, we have considered a 2-D approximation of each atoll shown in Fig. 5. The solid continental medium is considered as elastic without absorption and with an infinite quality factor. The bathymetry of both atolls is known with an error smaller than 10 m. The main geological units of the atoll structure are volcanic and carbonate formations. The thickness of the carbonate formation is known with an accuracy better than 50 m.

The finite difference modelling takes into account wave conversion in a discretized velocity-varying medium: the bathymetry is implicitly described by this variation on a grid. Whatever the numerical procedure for wave conversion, the key parameter for wave conversion will be the incident angle of the wave front. At each point M of the continental slope, hydroacoustic *T* waves are transmitted in seismic *P* or *S* waves when the incident angle $i(M)$ of the wave with respect to the continental slope is lower than critical angles i_{cp} and i_{cs} . The incident angle i decreases when the number of reflections between the sea surface and the seafloor increases. For both atolls, the highest slope is 30° near the top of the underwater cliff and decreases with depth. For such slopes, the hydroacoustic *T* waves need to be reflected once on the coral reef in order to be converted into seismic *P* waves.

5.1 Station FGA

Let us first analyse the synthetic particle velocity computed at FGA due to the seismic conversion of hydroacoustic *T* waves generated by a 200 m deep source. At this station, the envelope of the synthetic seismogram computed by the hybrid method is close enough to the real seismogram (Fig. 11) and makes us feel that our model structure is accurate enough for an interpretation of the phases. As shown by the synthetic polarization analysis (Fig. 12), the *P*-wave contributions are in the emerging part of the signal. The decreasing part and the coda (Rc) of the seismic *T* waves are composed of Rayleigh waves mainly created at the very top of the slope. Two main Rayleigh phases, denoted R1 and R2, are probably created at the top of the slope by the two hydroacoustic arrivals observed on the hydroacoustic synthetic signal in front of the coral reef (Fig. 6). These two Rayleigh phases may also be determined on the real records (Fig. 3). At FGA, located very close to the water at the top of the continental slope, the maximal *P* phase arrives just before the (R1) Rayleigh phase. The contribution of both waves may interfere with a higher amplitude than the amplitude that could be observed on a station further away. These results are in agreement with observation. Analysis by Talandier & Okal (1997) has shown that seismic *T* waves observed in French Polynesia are constructed with *P* waves and Rayleigh waves and that their amplitudes depend on the

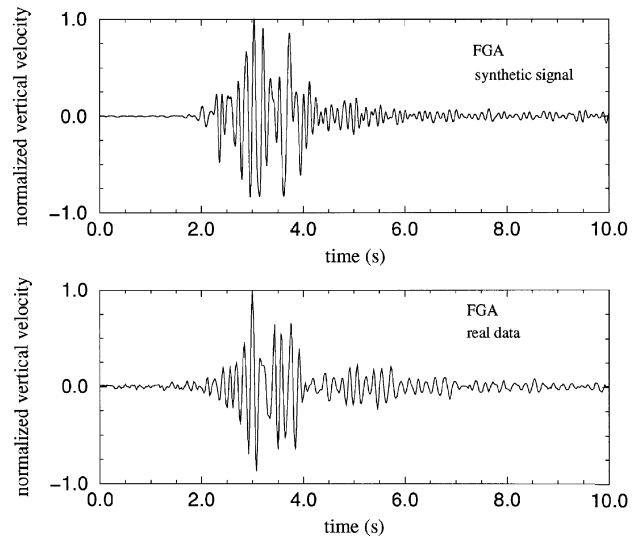


Figure 11. Comparison between synthetic and real seismograms at FGA. Both signals are normalized; origin times are arbitrary. The source time function is a unit normalized Ricker wavelet with main frequency equal to 6 Hz.

efficiency of the conversion along the continental slope. For a given range, the hydroacoustic *T*-wave duration is longer when the source is closer to the SOFAR channel axis. This relation is still valid for seismic *T* waves, as is shown on the synthetic signal that would be observed at FGA if the source depth were 500 m (Fig. 13). The signal duration is longer and its 4 s emergent part is very close to the synthetic hydroacoustic *T*-wave duration. The conversion phenomena may preserve the hydroacoustic *T*-wave duration, which is highly dependent on the depth of the explosive source. The observed seismic duration of the emergent part of the signal allows us to deduce the hydroacoustic *T*-wave duration and to estimate the source depth, although a careful analysis should be performed on each seismic station in order to estimate the influences of the top of the slope, the bathymetry of the atoll shores and the geological structure below the station position. Finally, the seismic *T*-wave energy due to a shallow source is lower than the seismic *T*-wave energy due to a source close to the SOFAR channel axis. Because continental wave conversion is very similar for both source depths, we have found that this relation observed for hydroacoustic propagation has been preserved for seismic propagation, although the energy conversion between the hydroacoustic and seismic waves is certainly complex.

5.2 Station DIN

Abrupt changes of the continental slope and distance variation between the top of the continental slope and the station may strongly change the shape of the seismic signal. The difference between observed signals at DIN and FGA may be explained by these two geometrical parameters. The synthetic signal computed at DIN (Fig. 14) is different from the signal computed at FGA. Because DIN is located 150 m away from the top of the continental slope and because the slope is only 6° at the top of the continental slope, the amplitude of the synthetic signal computed at this station is lower than the amplitude of the signal estimated at FGA. The duration and the emergent

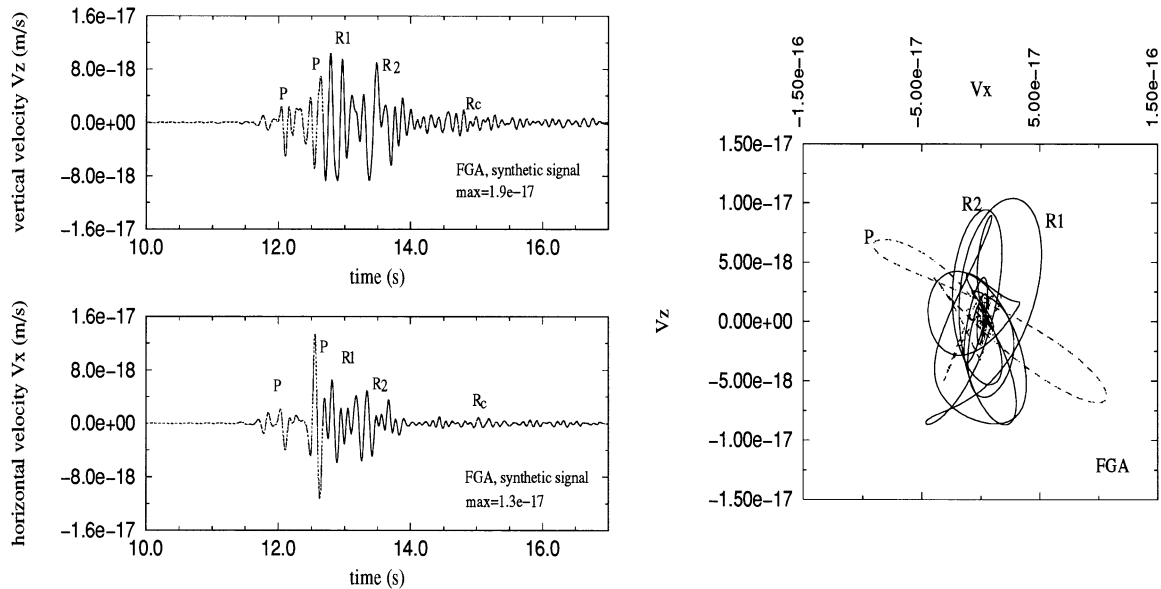


Figure 12. Synthetic seismic T waves computed at FGA at a distance of 981.5 km from a 200 m deep source, as done during the Midplate experiment. The source time function is a unit normalized Ricker wavelet with main frequency equal to 6 Hz. Phases are mainly P waves (P) and Rayleigh waves (R). The duration of the emergent part of the vertical component is 0.5 s. The synthetic vertical particle velocity V_z may be compared with the experimental data of Fig. 3. The maximum amplitude of the vertical particle velocity V_z is a Rayleigh phase, whereas the maximum amplitude of the horizontal particle velocity V_x is a P phase. The origin time is arbitrary.

part of the synthetic signal at DIN are still underestimated compared with the real signal.

We believe that this underestimation might come from 3-D effects which are more important for DIN than for FGA. In a 3-D continental model, rays would be laterally refracted and ray paths would be very different for a station far from the top of the continental slope. FGA is close enough to the top of the

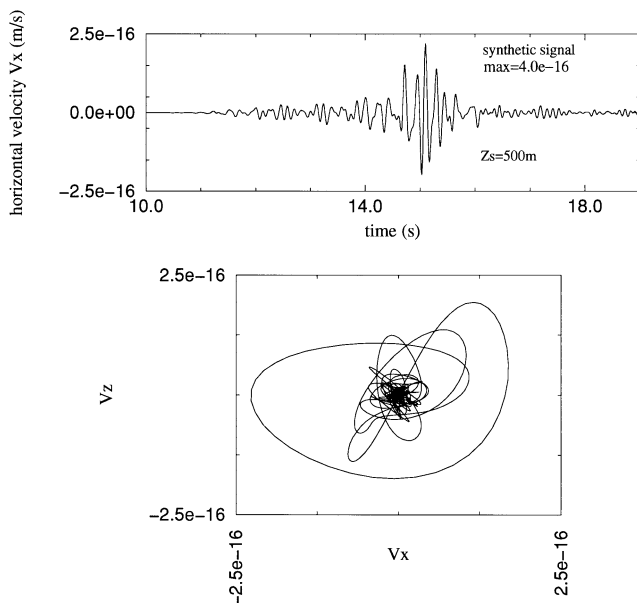


Figure 13. Synthetic seismic T waves computed at FGA. The hypothetical source is at 500 m depth. The source time function is a unit normalized Ricker wavelet with main frequency equal to 6 Hz. The duration of the emergent part of the signal is 4 s. The maximum amplitude of the vertical particle velocity V_z is a Rayleigh phase. Origin times are arbitrary.

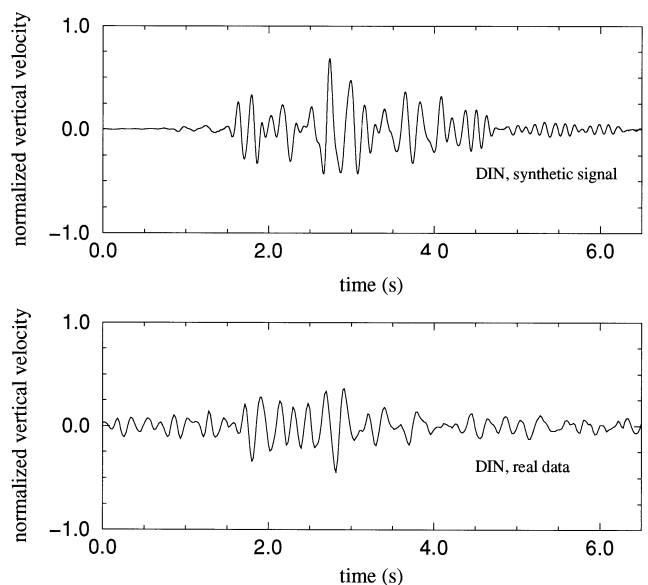


Figure 14. Comparison between synthetic and real seismograms at DIN. Synthetic seismic T waves computed at DIN at a distance of 944.3 km from a 200 m deep source. The synthetic signal and the real data are normalized in the same way as has been done at FGA (Fig. 11). Note that the amplitude at DIN is lower than the amplitude of the signal at FGA. The envelope shape of the synthetic data is different from the envelope shape of the real data because the 3-D contribution (not taken into account by the model) may be significant. Origin times of the two seismograms are arbitrary.

slope to make the 3-D contribution negligible, while for DIN 3-D ray paths might be longer and will increase the time duration and reduce the amplitude of the signal. This might be an explanation for the shorter duration and the higher amplitude of the synthetic signal computed at DIN compared to real data.

CONCLUSIONS

A hybrid method, coupling a global ray tracing approach and a finite difference technique, allows a study of the complete propagation of *T* waves from an underwater explosive source to a seismic receiver. As shown in this paper, this method is interesting for carrying out *T*-wave studies for earthquakes and explosions. This first study has illustrated the key role played by the source depth, the SOFAR channel propagation, the bathymetry of the continental slope and the distance of the receiver from the source and to the top of the continental slope. Our approach gives a straightforward interpretation of SOFAR channel propagation and may provide a phase identification as well as a source characterization capability. Therefore, this technique is particularly relevant for monitoring the Comprehensive Test Ban Treaty in oceans.

The envelope shape of a signal recorded at a long range on an underwater or a seismic receiver depends on the underwater source depth. The percentage of energy trapped in the SOFAR channel increases when the source gets closer to the channel axis. Therefore, the amplitudes of hydroacoustic and seismic *T* waves are dependent on the source depth. Unfortunately, the link between the source amplitude or the source depth and the receiver amplitude is complex. Even if two receivers are at the same distance from the source, the signal amplitude may be very different because of a change in the continental slope, or because of a change in the distance between the top of the continental slope and the station. Nevertheless, if it is possible to estimate the distance of the source, the signal duration recorded at a seismic receiver may help to provide a source depth evaluation.

When the source is close enough to the SOFAR channel axis and far enough from the receiver, it has also been shown that the signal duration at stations close to the channel axis may be considered to vary proportionally to distance. As a result, the signal duration of the hydroacoustic and seismic *T* waves increases with distance of oceanic propagation.

Although our approach is accurate in some cases and is a helpful tool for straightforward physical analysis, it needs to be studied in more detail. A more complete propagation modelling may be implemented taking into account oceanic and land absorption. A more important step consists of introducing a 3-D finite difference modelling to handle *T*-wave conversions at realistic 3-D continental slopes and shorelines.

ACKNOWLEDGMENTS

Gilles Lambaré and Prof. Hanyga are thanked for their significant contribution to the Maslov summation. Numerous scientific discussions with Yves Cansi and René Crusem are greatly appreciated. We also thank Frédéric Magniez for helping us to carry out the numerical modelling.

REFERENCES

Adams, R.D., 1979. T-phase recordings at Raratonga from underground nuclear explosions, *Geophys. J. R. astr. Soc.*, **58**, 361–369.
 Cansi, Y., 1981. Étude Expérimentale d'Ondes T, *Thèse*, Université de Paris-Sud.
 Cansi, Y. & Bethoux, N., 1985. T waves with long inland paths: synthetic seismograms, *J. geophys. Res.*, **90**, 5459–5465.
 Chapman, C.H., 1985. Ray theory and its extensions: WKBJ and Maslov seismograms, *J. Geophys.*, **58**, 27–43

Ewing, W.M. & Worzel, J.L., 1948. Long range transmission, *Geol. Soc. Am. Mem.*, **27**.
 Farra, V. & Madariaga, R., 1987. Seismic waveform modeling in heterogeneous media by ray perturbation theory, *J. geophys. Res.*, **92**, 2697–2712.
 George, T., Mechler, P. & Stephan, Y., 1994. Acoustic modelling in SOFAR: application to interpretation of GASTOM 90, *Proc. Ocean '94 Congress*.
 Gibowicz, S.J., Latter, J.H. & Sutton, G.K., 1974. Earthquake swarm associated with volcanic eruption, Curacao Reef, Northern Tonga, July 1973, *Ann. Geofis.*, **27**, 443–475.
 Huang, X. & West, G.F., 1997. Effects of weighting function on the Maslov uniform seismograms: a robust weighting method, *Bull. seism. Soc. Am.*, **87**, 164–173.
 Jensen, F.B., Kuperman, W.A., Porter, M.B. & Schmidt, H., 1994. *Computational Ocean Acoustics*, American Institute of Physics Press, New York, NY.
 Kravtsov, Yu.A., 1968. Two new asymptotic methods in the theory of wave propagation in inhomogeneous media (review), *Soviet Physics—Acoustics*, **14**, 1–24.
 Leray, J., 1972. *Solutions Asymptotiques des Équations aux Dérivées Partielles (une Adaptation du Traité de V. P. Maslov)*, Convegno Internazionale Metodi Valuativi nella Fisica Matematica, Rome.
 Maslov, V.P., 1965. *Perturbation Theory and Asymptotic Methods*, Moskov. Gos. Univ., Moscow (in Russian).
 Piserchia, P.F., Virieux, J., Rodrigues, D. & Lambaré, G., 1997. Numerical modelling of oceanic acoustic wave propagation, *J. acoust. Soc. Am.*, submitted.
 Porter, R.P., 1973. Dispersion of axial SOFAR propagation in the western Mediterranean, *J. acoust. Soc. Am.*, **53**, 181–191.
 Rodrigues, D., 1993. Large scale modeling seismic wave propagation, *thèse*, Ecole Centrale Paris.
 Rodrigues, D., 1996. Théorème de Représentation, théorie et application aux champs téléseismiques, aux sources non-linéaires et aux explosions atmosphériques, *Internal Rept*, Laboratoire de Détection et de Géophysique, Bruyères-Le-Chatel, France.
 Spiesberger, J.L., 1994. Successful ray modeling acoustic multipaths over 3000 km section in the Pacific, *J. acoust. Soc. Am.*, **95**, 3654–3657.
 Talandier, J., 1990. Midplate II (7 to 28 December 1989), *Preliminary report*, Laboratoire de Détection et de Géophysique.
 Talandier, J. & Okal, É., 1987. Seismic detection of underwater volcanism: the example of French Polynesia, *Pure appl. Geophys.*, **125**, 919–950.
 Talandier, J. & Okal, É., 1996. Monochromatic T waves from underwater volcanoes in the Pacific Ocean: ringing witnesses to geyser process, *Bull. seism. Soc. Am.*, **86**, 1529–1544.
 Talandier, J. & Okal, É., 1997. On the mechanism of conversion of seismic waves to and from *T*-waves in the vicinity of islands, *Bull. seism. Soc. Am.*, in press.
 Thomson, C.J. & Chapman, C.H., 1985. An introduction to the Maslov asymptotic method, *Geophys. J. R. astr. Soc.*, **83**, 143–168.
 Urick, R.J., 1982. *Sound Propagation in the Sea*, Peninsula Publishing, Las Altos.
 Virieux, J., 1991. Fast and accurate ray tracing by Hamiltonian perturbation, *J. geophys. Res.*, **96**, 579–594.
 Virieux, J. & Farra, V., 1991. Ray tracing in 3-D complex isotropic media: an analysis of the problem, *Geophysics*, **16**, 2057–2069.
 Virieux, J., Farra, V. & Madariaga, R., 1988. Ray tracing for earthquake location in laterally heterogeneous media, *J. geophys. Res.*, **93**, 6585–6599.
 Weigel, W., 1990. *Bericht über die SONNE-Expedition SO 65-2, Papeete—Papeete, 7 Dezember—28 Dezember 1989*, Institut für Geophysik, Universität Hamburg.
 Worcester, P.F., 1981. An example of ocean multipath identification at long range using both travel time and vertical arrival angle, *J. acoust. Soc. Am.*, **70**, 1743–1747.
 Ziolkowski, R.W. & Deschamps, G.A., 1984. Asymptotic evaluation of high-frequency fields near a caustic: an introduction to Maslov's method, *Radio Sci.*, **19**, 1001–1025.